Efficient Ultrafast Scintillation of KLuS$_2$:Pr^{3+} Phosphor: A Candidate for Fast-Timing Applications

V. Jarý[1,*] L. Havlák,[1] J. Bárta,[1,2] E. Mihóková,[1] R. Kučerková,[1] M. Buryi,[1] V. Babin,[1]
P. Průša,[1,2] T. Vrba,[2] A. Kotlov,[3] and M. Nikl[1]

[1]*Institute of Physics, Czech Academy of Sciences, Cukrovarnicka 10, 16200 Prague, Czech Republic*

[2]*Faculty of Nuclear Sciences and Physical Engineering, Czech Technical University in Prague, Brehova 7, Praha 1, Prague 11519, Czech Republic*

[3]*PETRA III, Beamlines, P66 Superlumi, Deutsches Elektronen-Synchrotron DESY, Notkestr. 85, 22607 Hamburg, Germany*

A set of Pr^{3+}-doped KLuS$_2$ samples with different Pr concentrations are synthesized in the form of transparent crystalline hexagonal platelets by chemical reaction under a flow of hydrogen sulfide. Their structural, optical, and scintillation properties are investigated thoroughly by means of x-ray powder diffraction, time-resolved luminescence spectroscopy, scintillation light yield, and decay measurements to assess the spectroscopic properties of Pr^{3+} ions in the KLuS$_2$ host. Charge-trapping processes are further investigated by electron paramagnetic resonance. The fundamental absorption band edge of the KLuS$_2$ host is located at 303 nm, the absorption due to the Pr^{3+} $4f \rightarrow 5d$ transition is found at 347 nm, the emission maximum is given by the $4f$ $^1 5d1 \rightarrow {}^3H_4$ transition of the Pr^{3+} ion at 380 nm, and the leading photoluminescence and scintillation decay time is around 1 ns at room temperature. The moderate scintillation light yield reaches 7200 ph/MeV. A phenomenological model is fitted to the measured temperature dependences of the photoluminescence emission spectra and photoluminescence decay times to better understand the dynamics of the $5d$ excited state of the Pr^{3+} center in the KLuS$_2$ host. The number of photons emitted in the first nanosecond of the scintillation response is evaluated and found to be considerably higher (1.6–2.5 times) than that in the commercial (Lu;Y)$_2$(SiO$_4$)O:Ce, Ca scintillator, which shows the potential of Pr-doped KLuS$_2$ for fast-timing scintillator applications.

I. INTRODUCTION

Worldwide, there are many inorganic hosts with many different functionalities when doped by different activators, many of which are rare-earth ions, such as Ce^{3+}, Eu^{2+}, Pr^{3+}, and others. One of the best known is Y$_3$Al$_5$O$_{12}$, commonly designated as YAG (yttrium-aluminum-garnet). Ce^{3+}-doped YAG is one of the most famous scintillating materials with favorable properties, such as fast scintillation decay time, relatively high light yield, high mechanical resistance, and easy and cheap fabrication method [1–4]. At the same time, when YAG:Ce^{3+} is attached to a blue pumping light-emitting diode (LED), the most used solid-state white-light source is constructed, and nowadays it can be found basically in every cell-phone flashlight [5–7]. When other dopants, such as Nd^{3+} [8–10], Er^{3+} [11,12], or Yb^{3+} [13,14], are incorporated into the YAG host, famous solid-state laser materials are created. Similarly, the KLuS$_2$ host appears to be highly promising material as well; when doped with Tm^{3+} or Yb^{3+} ions, low-phonon materials suitable for mid-IR lasers are obtained [15]. Using Raman spectroscopy, it is found that the KLuS$_2$ phonon energy is $E_{ph} \approx 220$ cm^{-1}, which is fully comparable to the best low-phonon materials currently investigated for mid-IR lasers, such as KPb$_2$Cl$_5$ [16], YCl$_3$ [17], and others [18]. More interestingly, Eu^{2+}-doped KLuS$_2$ was discovered and described in 2013 [19]. By using the electron paramagnetic resonance (EPR) technique, it is proved that approximately 50% of Eu^{2+} ions occupy the K$^+$ site, while the other 50% occupy the Lu^{3+} site, through which a natural charge compensation can be reached [20]. Phosphor classes derived from KLuS$_2$:Eu^{2+} appear to have a high application potential in the field of tunable solid-state white LED sources [21–24]. Furthermore, a strategy to codope KLuS$_2$:Eu^{2+}

*jary@fzu.cz

with Pr^{3+}, Ce^{3+}, or Sm^{3+} is proposed to improve the color properties of given phosphors [25]. Finally, Ce^{3+}-doped $KLuS_2$ appears to be of interest in the field of x-ray and γ-ray scintillating convertors [26,27], mainly due to the elevated effective atomic number ($Z_{eff} = 59$ [27]) and density ($\rho = 4.69$ g cm^{-3} [27]), efficient energy transfer from the host to the Ce^{3+} centers, lower band gap (relative to oxide-based materials), and light yield exceeding 23 000 ph/MeV with almost no slow components in the scintillation response within the 0.5–10 μs shaping time [26,27]. Global interest in the $KLnS_2$ host (where Ln denotes lanthanoids) is also demonstrated by an increasing number of theoretical studies devoted to its various characteristics. Structural, elastic, electronic, and optical properties of $KLnS_2$ (Ln = Y and La) using *ab initio* calculations based on the density-functional theory, including calculations of unit-cell volumes, bulk modulus, Debye temperature, and heat capacities, are presented in Ref. [28]. Similarly, based on *ab initio* calculations, the structural, elastic, electronic, and optical properties of $KEuS_2$ were studied in Ref. [29]. Dielectric function, reflectivity, and loss functions are discussed in detail. Selenides [30,31] and tellurides [32,33] started to be investigated theoretically as well, mainly for their promising optical, elastic, and magnetic properties.

Recently, structural determinations of rhombohedral $ALnS_2$ (Ln = La, . . . Lu) [34–37] (space group $R\text{-}3m$, no. 166) were published and indicated a systematic error in previous structure determinations, notably the position of S^{2-} at Wyckoff position 6c in this group [0,0,z]. The fractional coordinate z (S^{2-}) in alkali rare-earth sulfides is a good parameter for simple monitoring of structural trends (see Fig. 6 in Ref. [34], Fig. 2 in Ref. [36], and Fig. 9 in Ref. [35]).

Scintillating materials based on inorganic crystals are nowadays ordinarily used for the detection of ionizing radiation in medical imaging, dosimetry, and high-energy physics [1, and references therein]. In recent years, the fast-timing capability, in particular, has received attention because of time-of-flight applications, such as positron emission tomography [38–41]. The timing capability of the material is quantified by the so-called coincidence time resolution (R_{CT}), where $R_{CT} \sim (\tau_r \tau_d / N_{PHP})^{1/2}$, with N_{PHP} being the number of detected photoelectrons per 511 keV of absorbed annihilation photons and τ_r and τ_d representing the scintillator's rise time and decay time, respectively. Therefore, for a good timing resolution, inorganic scintillators with a high scintillation light yield (Y_l) and a short decay time, τ_d, are needed, as in the first approximation the photon density is given by Y_l / τ_d. In addition, the rise time, τ_r, delays the emission and the conversion of the first produced photons. Typical R_{CT} values for widely used standard scintillators are currently in the order of 100 ps or higher [42,43]. A few approaches are identified to provide a photon time density in the leading edge of the

scintillation pulse compatible with a desired 10-ps R_{CT} target. Strong efforts must therefore be made to improve the timing performance of existing scintillators to get the highest light yield and/or the shortest rise and decay times [44]. Here, we propose a single-crystalline scintillator employing fast $5d \rightarrow 4f$ emission of the Pr^{3+} ions in ternary sulfides. As already mentioned, $KLuS_2$ possesses several intrinsic advantages for use in x-ray and γ-ray detection. The aim of the following work is to characterize carefully the optical, structural, and magnetic properties of the Pr^{3+} emission center in the $KLuS_2$ host by employing simultaneously time-resolved luminescence spectroscopy and electron paramagnetic resonance. Such a combination of these two techniques already proved to be very efficient in characterizing interesting materials, for example, in the case of Cs_2HfCl_6 [45]; Eu^{2+}-doped YAG [46]; or, as already mentioned, Eu^{2+}-doped $K_xNa_{1-x}LuS_2$ [24].

II. SAMPLE PREPARATION

The Pr-doped or undoped $KLuS_2$ crystalline samples are synthesized according to the diagram given in Ref. [47]. The starting materials are 99.997% K_2CO_3, 99.999% Lu_2O_3, and 99.999% Pr_6O_{11} (for $KLuS_2$:Pr 0.05%). The gases used during synthesis are 99.999% Ar and 99.5% H_2S. The chemical reactions are carried out in a corundum tube (99.7% Al_2O_3). The tube is placed in an electric resistance furnace equipped with heating- and cooling-rate regulation. Either Ar or H_2S gas is allowed to flow into the reaction tube. The gases are taken directly from pressurized cylinders using a three-way stopcock to switch between them. A mixture of K_2CO_3 and Pr-doped or undoped Lu_2O_3 in a molar ratio of 80:1 is used as the starting material. Pr doping is carried out by simple mixing and grinding of Lu_2O_3 and Pr_6O_{11}.

Prior to the reaction itself, the reagents (K_2CO_3 and Lu_2O_3:Pr_6O_{11} or undoped Lu_2O_3) are homogenized in an agate mortar. The mixture is placed in a corundum boat (99.7% Al_2O_3) and inserted into the corundum tube (inner volume about 1 dm^3). The mixture is then heated to 1323 K using the electric resistance furnace (heating rate 10 K/min) under a flow of Ar (30 dm^3/h). After the desired temperature is reached, the reaction mixture is annealed for 2 h under a flow of H_2S (15 dm^3/h). Following annealing, the system is cooled under a flow of Ar (0.5 K/min, 0.3 dm^3/h). The volume flow rate is measured before the gases enter the tube under normal conditions (normal pressure about 101 kPa and normal temperature about 293 K). The volume flow rate of H_2S 15 dm^3/h is equivalent to a mass flow rate of 21.2 g H_2S/h. The volume flow rate of Ar 30 dm^3/h is equivalent to a mass flow rate of 49.7 g Ar/h (or 0.5 g Ar/h in the case of 0.3 dm^3 Ar/h). Upon reaching room temperature, the corundum boat is removed from the tube furnace and the reaction products are purified by suspension and decantation, three

times with distilled water and once with acetone. K_2S is removed by water, while pure or Pr-doped $KLuS_2$ samples are left behind. The resulting products consist of about 40-µm-thick platelets with imperfect hexagonal morphology sized up to 3×4 mm². For more details, see also Refs. [15,19,21–27,47–49].

The produced material is then manually separated into a fraction of large platelets, which are observed to always be phase-pure $KLuS_2$ sulfides, and a fraction of small crystals or powder. In the fraction of small platelets, a very stable Lu_2O_2S oxysulfide phase can be present in powder form when the synthesis conditions are not optimized. Therefore, it can be stated that compounds based on $KLuS_2$ are—when not ground—stable in air, and even after many years, no changes to the surface are observed [15,19,21–27,47–49].

$Bi_4Ge_3O_{12}$ (BGO) and $(Lu;Y)_2(SiO_4)O$ (LYSO:)Ce, Ca are commercial single-crystal standards obtained from different companies (Shonan Institute of Technology, Fujisawa for BGO, Proteus for LYSO:Ce, Ca), and their dimensions are approximately $5 \times 5 \times 1$ mm³.

III. EXPERIMENTAL SETUP

The phase purity of the samples is verified by x-ray powder diffraction using a Rigaku MiniFlex 600 diffractometer equipped with a copper anode [40 kV, 15 mA; $\lambda(Cu\ K\alpha1,2) = 1.54184$ Å], nickel $K\beta$ filter, and NaI : Tl scintillation detector. The small crystals are pressed into glass holders (0.2-mm depression) without any grinding step to limit possible surface oxidation. The diffraction patterns are recorded within $2\theta = 10–80°$ in continuous mode at a scanning rate of 2°/min and analyzed using the PDXL2 software. The observed diffraction peaks are indexed and both the lattice parameters in the hexagonal setting and sample displacement are determined from their positions. The presence of phase impurities is checked using the ICDD PDF-2 database (version 2013) [50].

Absorption spectra are measured using the ultraviolet–visible–near-infrared Shimadzu 3101PC spectrophotometer in the range of 190–3200 nm. Radioluminescence (RL), photoluminescence excitation (PLE), and photoluminescence emission (PL) spectra connected with PL decay curves are measured by a custom-made 5000M spectrofluorometer (Horiba Jobin Yvon, Wildwood, MA, USA) using the Mo x-ray tube (40 kV, 15 mA, Seifert), steady-state xenon lamp (EQ-99X LDLS-Energetic, a Hamamatsu Company), and nanosecond nano-LED pulsed light sources (fast prompt decay curves measured by the time-correlated single-photon counting technique, Hamamatsu) as the excitation sources. The detection part of the setup involves a single-grating monochromator and a photon-counting TBX-04 detector (Hamamatsu). Measured spectra are corrected for the spectral dependence of detection sensitivity (RL, PL, PLE). The convolution procedure is applied to the photoluminescence decay curves to determine true decay times (SpectraSolve software package, Ames Photonics). Measurements of the optical characteristics within the 77–320-K temperature regions are performed using a liquid-nitrogen bath cryostat [Oxford Instruments, UK (Oxford)]. For every RL spectrum, the BGO standard crystal scintillator is measured under the same geometrical conditions as well to obtain quantitative intensity information. Experimental setups are schematically shown in Figs. S1 and S2 within the Supplemental Material [79]. Figure S1 shows the setup for measuring photoluminescence excitation and photoluminescence emission spectra, Fig. S2 shows the setup for measuring photoluminescence decay curves, and Fig. S3 shows the setup intended to measure radioluminescence spectrum.

The measurements of emission and excitation spectra, as well as luminescence decay kinetics, are performed at the SUPERLUMI station of the P66 beamline at DESY under pulsed excitation by synchrotron radiation in the range of 30–330 nm from the PETRA III storage ring. The excitation monochromator is of 2-m normal incidence McPherson type equipped with a holder for two Al and Pt interchangeable gratings. The Al grating has 1200 lines/mm and is optimized for the spectral range of 100–330 nm, blazed at 180 nm; the Pt grating has 1200 lines/mm, blazed at 55 nm, and intended for the spectral range of 30–100 nm. Excitation spectra are measured with an instrumental resolution of about 0.3 nm. Luminescence spectra in the UV and visible range (200–1100 nm) are recorded with a Czerny-Turner-type Kymera 328i spectrograph (Andor) equipped with a cooled CCD Newton 920 detector. The analyzing monochromator is equipped with three interchangeable 300 lines/mm gratings blazed at 300, 500, and 1200 nm. For measurements of excitation spectra and for time-resolved measurements, the luminescence is detected by a photomultiplier (Hamamatsu R6358) working in the 185–830-nm range with a time resolution of about 1 ns or by a photomultiplier microchannel plate (Hamamatsu R3809U) working in the range of 160–850 nm with a time resolution of about 55 ps. The detectors are attached to the second exit port of the same spectrograph. The set of long-pass sharp cutoff filters is also available for the detection line. The samples are located on the cold finger of the He-flow cryostat, enabling temperature regulation in the range of 15–300 K. All luminescence spectra are corrected for the quantum efficiencies of the CCD camera and gratings. The excitation spectra are corrected using sodium salicylate.

The fast x-ray-excited spectrally unresolved scintillation decays are measured at room temperature by the time-correlated single-photon-counting method using a Fluoro-Hub unit coupled with a hybrid photomultiplier (Horiba Jobin Yvon) together with the picosecond x-ray pulsing source at 40 kV (Hamamatsu). The instrumental response function of the setup is 75 ps.

The scintillation light yield is given by $Y_l = Y_{pe}/(\eta_{QE} \times \eta_{CE})$, where Y_{pe} is the photoelectron yield, i.e., the number of collected photoelectrons per MeV of absorbed energy; η_{QE} is the quantum efficiency of a photodetector; and η_{CE} is the light-collection efficiency. Unfortunately, we are not able to precisely determine η_{CE} for the sample studied, due to the irregular shape and surface. Therefore, we present the light-yield estimate, $Y_{l,e} = Y_{pe}/\eta_{QE} \le Y_l$, instead. Y_l equals $Y_{l,e}$ only for $\eta_{CE} = 1$. Considering the sample absorption, low thickness, and application of optical grease and reflector, η_{CE} is as close to unity as possible for the material studied.

The scintillation light-yield estimate ($Y_{l,e}$) is determined by pulse-height spectroscopy of the scintillation response [51], using a hybrid photomultiplier (HPMT) [52], model DEP PPO 475C; an ORTEC spectroscopy amplifier, model 672 (shaping time $t = 1$ μs); and an ORTEC 927TM multichannel buffer. Low-energy γ-rays from ^{57}Co (122 keV), ^{241}Am (59.5 keV), ^{129}I (29.8 keV), ^{109}Cd (22.2 keV), and ^{55}Fe (5.9 keV) are used for excitation due to small sample dimensions. The sample is optically coupled to the HPMT using silicon grease; more than 10 layers of Teflon tape are used as a reflector. Higher γ-ray energies cannot be used, since the samples are very thin (approximately 0.1 mm). All measurements are performed at room temperature.

Please note that the shaping time, $t = 1$ μs, allows only photons of the fast component to significantly contribute to the pulse height. Therefore, it is correct to present only the Y_l of the fast component and its estimate. These quantities are denoted as $Y_{l,f}$ and $Y_{l,f,e}$, respectively. $Y_{l,f,e}$ is determined as follows. First, the number of collected photoelectrons, N_{PHEL}, is obtained from the Gaussian fit of the photopeak in the pulse-height spectra, calibrated in photoelectron equivalents. The response of 1, 2, 3, and even 10 photoelectrons can be observed in the HPMT pulse-height spectra of low-intensity light source, as shown in Fig. S4 within the Supplemental Material [79]. Such a spectrum is very convenient for calibration of the pulse-height spectra in photoelectron equivalents. The photoelectron yield, $Y_{pe,f} = N_{PHEL}/E$, where E is the absorbed energy delivered by the ionizing-radiation particle, e.g., gamma photon. The spectral dependence of the quantum efficiency, $\eta_{QE}(\lambda)$, is determined by the HPMT supplier. η_{QE} for both samples is calculated using RL spectra, as a weighted average of $\eta_{QE}(\lambda)$, where RL intensity, $I(\lambda)$, for a given wavelength, λ, is the weighing factor:

$$\eta_{QE} = \sum_\lambda I(\lambda)\eta_{QE}(\lambda). \qquad (1)$$

Finally, the light-yield estimate is calculated: $Y_{l,f,e} = Y_{pe}/\eta_{QE}$.

Spectra of absorbed energy (inside samples) are calculated by the Monte Carlo method using MCNP 6.2, tally F8 [53]. The simulation geometry is simplified, as the real samples are shaped irregularly. In the simulation, the sample is approximated by a perfect cylinder with a diameter of 4 mm and height of 0.1 mm. The point source of radiation is placed at the sample axis, at the distance of 2 mm. The sample is lying on a SiO$_2$ cylinder (HPMT window), Ø 50 mm, height 2 mm. The surroundings are filled with air. The bin width is 0.5 keV. Light collection is not simulated. Please note that MCNP simulations are performed only as a tool for the identification of peaks in the pulse-height spectra. Otherwise, it would be problematic due to the presence of escape peaks and very low detection efficiency, especially for higher energies of ionizing radiation. For such purposes, the geometry simplification is justifiable.

EPR measurements are performed with a commercial Bruker EMXplus spectrometer in the X band (9.4 GHz, resonator type ER4122SHQE, TE011 mode) within the 4–296-K temperature range using an Oxford Instruments ESR900 cryostat. The sample is placed in a quartz tube. The x-ray irradiation of the sample (in the quartz tube) is performed at 77 K, the liquid-nitrogen temperature, using ISO-DEBYEFLEX 3003 highly stabilized x-ray equipment for structure analysis (tungsten x-ray tube, 50 kV, 30 mA). The analysis of the EPR spectra is done in the Easyspin 5.2.35 toolbox program.

IV. RESULTS AND DISCUSSION

The diffraction pattern of the small platelets of KLuS$_2$:Pr 0.05% confirm that the sample consists only of the rhombohedral KLuS$_2$ phase, see Fig. 1. Due to the shape and crystallographic orientation of the platelets, the diffraction patterns of such samples are completely dominated by the (0 0 3n) family of diffraction lines, even when intense grinding is applied; destructive incorporation into a suitable glue material can decrease this preferred orientation effect. The intensity of other KLuS$_2$ diffraction
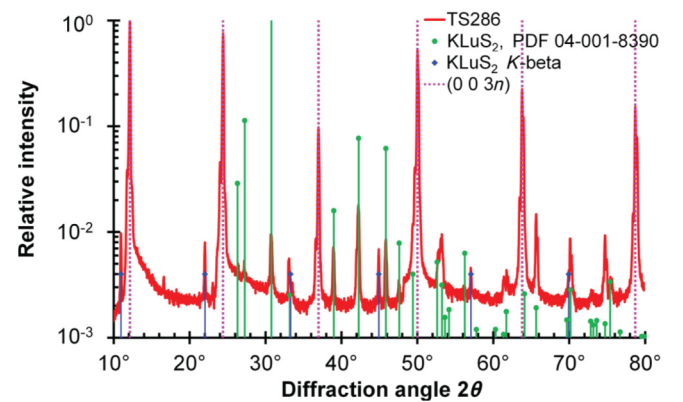

FIG. 1. Powder x-ray diffraction spectrum of KLuS$_2$:Pr 0.05%; (0 0 3n) lines are doubled due to a small fraction of the sample being vertically displaced by $s = -0.24(6)$ mm; $K\beta$-filter-caused cutoff of the spectrum diffracted from the sample is clearly visible for these lines as well at the low-angle side.
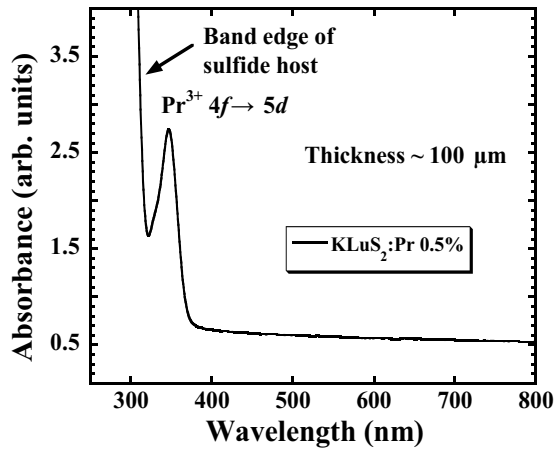
FIG. 2. Room-temperature absorption spectrum of KLuS$_2$:Pr 0.5%.

lines is even smaller than the residual Cu $K\beta$ lines of (0 0 3n), and no diffraction lines of possible impurity phases are observed. The determined lattice parameters of the KLuS$_2$:0.05% Pr sample (fraction of small particles), $a = 3.955(4)$ Å and $c = 21.867(5)$ Å, are, within experimental uncertainties, identical to the lattice parameters of KLuS$_2$:Eu reported earlier [24].

The room-temperature absorption spectrum of KLuS$_2$: Pr 0.5% is shown in Fig. 2. Two clear structures can be seen. The fundamental band gap of KLuS$_2$ host is located at around 300 nm, in agreement with previously reported data [19,26,27]. At lower energies, the fully allowed Pr^{3+} $4f \rightarrow 5d$ transition is well resolved and visible, peaking at 347 nm. No characteristic Pr^{3+} $4f \rightarrow 4f$ absorption lines are visible in the 400–800-nm region, probably due to the limited thickness of the sample and their forbidden nature. It is to be noted that in previous studies the authors

claimed that a similar absorption band in the Pr^{3+}-doped RbLaS$_2$ could be attributed to the S$^{2-} \rightarrow$ Pr^{3+} charge-transfer transition, as it is expected that the Pr^{3+} $4f \rightarrow 5d$ absorption will be above the band gap at 290 nm [47,54]. Furthermore, an analogous ligand-to-Pr^{3+} charge-transfer transition is ascribed to the 240- and 320-nm excitation bands in Pr-doped LuCl$_3$ and LuI$_3$, respectively [55,56]. The mentioned excitation band, however, is not studied further, as Pr^{3+} $5d \rightarrow 4f$ emission is not observed at all in the RbLaS$_2$ host at room temperature [47].

A. Scintillation properties

The room-temperature RL spectrum of KLuS$_2$:Pr 0.05% is shown in Fig. 3(a), together with the reference BGO single-crystal scintillator. Two emission regions can be distinguished in the spectrum. At the higher-energy side, the Pr^{3+} $4f^{1}5d^{1} \rightarrow {}^{3}H_4$, $4f^{1}5d^{1} \rightarrow {}^{3}H_5$, and $4f^{1}5d^{1} \rightarrow {}^{3}F_{2,3}$ transitions (generally called $5d \rightarrow 4f$ transitions) can be assigned to the bands at 377, 405, and 452 nm, respectively. Data are taken from Ref. [59]. At the lower-energy side, between 480 and 800 nm, the partially relaxed parity-forbidden $4f \rightarrow 4f$ transitions of Pr^{3+} ions are located. KLuS$_2$ host emission, typically peaking at around 430 nm [27], is not visible in the spectrum, which points to an efficient energy transfer from the KLuS$_2$ host to the Pr^{3+} emission center. The RL spectra integral for KLuS$_2$:Pr 0.05% (integrated in the 310–480-nm region, where the fast $5d \rightarrow 4f$ emission is peaking) compared to that of the BGO standard scintillator (integrated in the 310–800-nm region) shows that KLuS$_2$:Pr 0.05% provides 190% of the BGO intensity at room temperature. Similarly (not shown), the KLuS$_2$:Pr 0.5% sample provides 320% of the BGO intensity at room temperature. At 77 K,

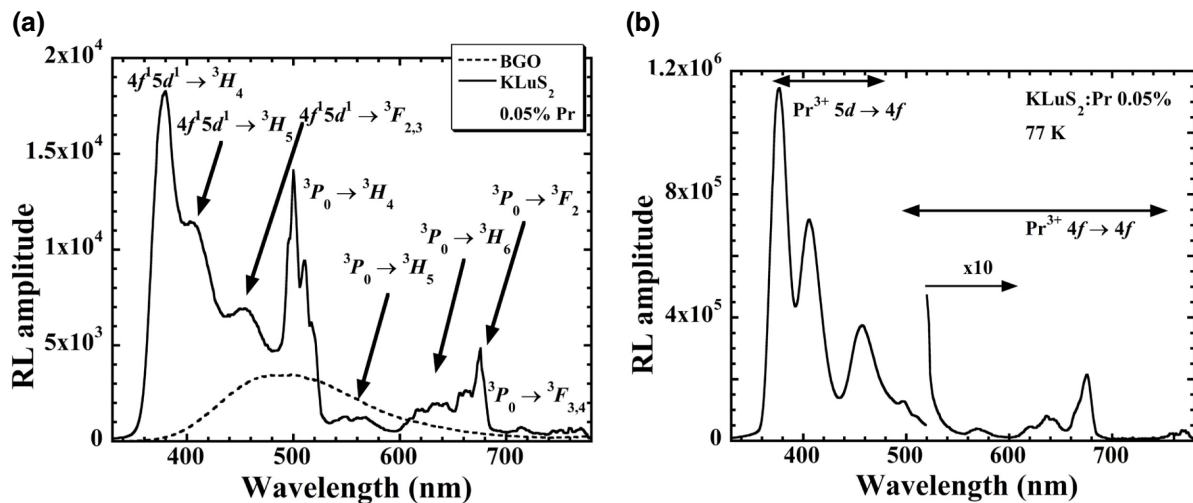FIG. 3. Radioluminescence spectra of KLuS$_2$:Pr 0.05% [57,58] measured at room temperature (a) and 77 K (b); RL amplitude in the 520–800-nm region is multiplied by 10 for better clarity.
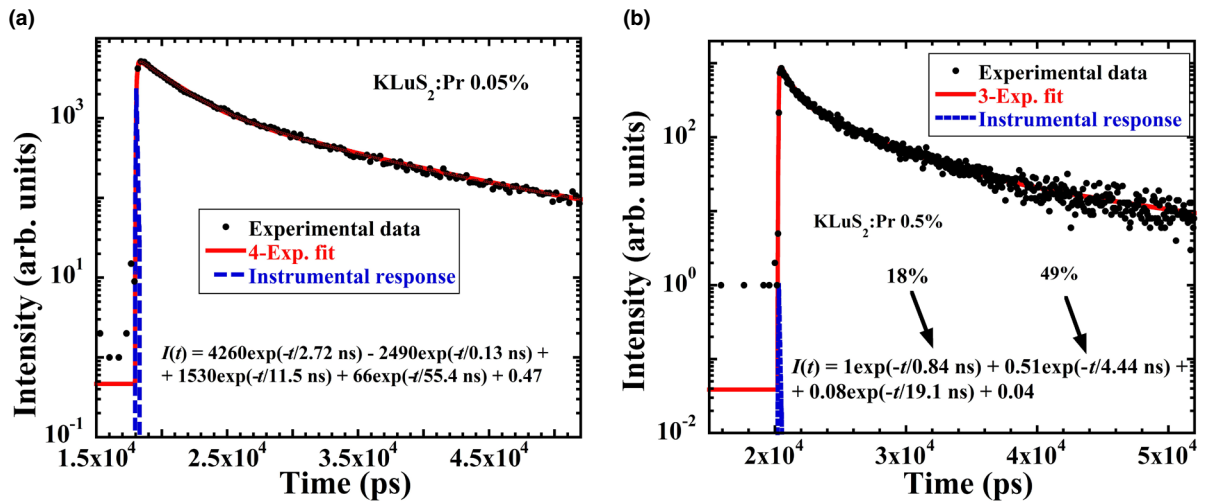
FIG. 4.   (a) Room-temperature scintillation decay of KLuS$_2$:Pr 0.05%; (b) scintillation decay of KLuS$_2$:Pr 0.5%. Solid line is a convolution of the instrumental response and function $I(t)$ in the figure.

see Fig. 3(b), emission bands in the RL spectrum corresponding to the $5d \rightarrow 4f$ emission of Pr^{3+} become better resolved, and they start to dominate over the Pr^{3+} $4f$-$4f$ transitions [note that the intensity of the RL spectrum in Fig. 3(b) in the 520–800-nm region is multiplied by 10]. When the RL spectra of KLuS$_2$:Pr^{3+} 0.5% are measured at room temperature and 77 K using identical experimental and geometrical conditions, it can be stated that the RL intensity at room temperature reaches 15% of that at 77 K.

Figures 4(a) and 4(b) show the spectrally unresolved scintillation decay of KLuS$_2$:Pr 0.05% and KLuS$_2$:Pr 0.5% excited by 40-kV x-ray pulses of 75-ps FWHM. The decay curves are approximated by the sum of four [Fig. 4(a)] or three [Fig. 4(b)] exponentials in the following form [Eq. (2)]:

$$I(t) = \sum_{i=1}^{3,4} A_i e^{-t/\tau_i} + \text{background}, \qquad (2)$$

where A_i and τ_i are the amplitude of the ith component and decay time of the ith component, respectively. The portion of light released by the ith component, which is commonly called a light sum ($L_{s,i}$), can be calculated as

$$L_{S,i} = \frac{A_i \tau_i}{\sum_{i=1}^{3,4} A_i \tau_i}, \qquad (3)$$

the values of which are also to be found in Figs. 4(a) and 4(b). Therefore, in the case of the KLuS$_2$:0.5% Pr sample, more than 70% of the scintillation light is released within 5 ns after the excitation pulse, which makes the KLuS$_2$:Pr^{3+} material one of the fastest emitters in the class of inorganic bulk crystalline scintillating materials. In the case of the KLuS$_2$:0.05% sample, the situation is more

complex, since the rise time is present. This may indicate an energy transfer to the $5d$ Pr^{3+} excited state and will be studied further in the future. For comparison, the luminescence decay of the KLuS$_2$:Pr 0.05% sample is also measured using synchrotron radiation with a wavelength of 40 nm as the excitation source, thus high above the band gap. This decay curve can be seen in Fig. S5 within the Supplemental Material [79]. However, observed decay, in both cases, is significantly accelerated from what is usually expected from the Pr^{3+} $5d \rightarrow 4f$ transition [60]. This may indicate a certain degree of thermal quenching, see below.

A representative afterglow curve measured for the KLuS$_2$:Pr 0.5% sample is displayed in Fig. 5. The sample is continuously irradiated by the x-ray source (40 kV, 15 mA) for a few tens of seconds. Then, the excitation source is cutoff and the spectrally unresolved emission (emission monochromator is set to 0, and therefore, all
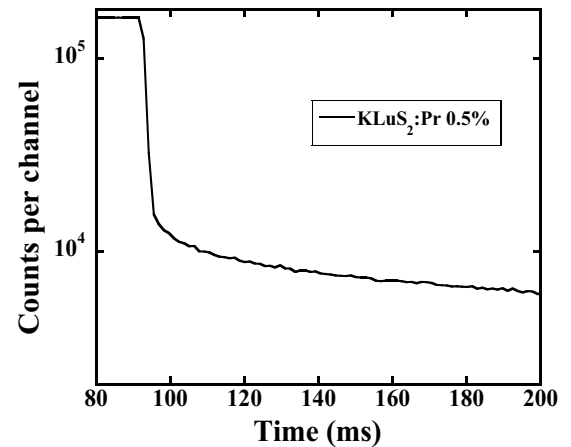

FIG. 5.   Room-temperature spectrally unresolved afterglow curve of KLuS$_2$:Pr 0.5% ($E_x = 40$ kV x-ray).

the light coming to the PMT is detected) is monitored over time with approximately 1.3-ms steps. The measure of afterglow is expressed by the percentage of photons emitted 3 ms after the continuous x-ray-radiation cutoff, with a desirable value of <0.1% [61,62]. One can see from Fig. 5 that there is a significant drop in the intensity down to 7% approximately 10 ms after the x-ray cutoff followed by a further mild decrease over a longer timescale. As the afterglow is generally considered to be harmful to the scintillator performance, there is huge room for further improvement of KLuS$_2$:Pr to become comparable to well-known low-afterglow materials like BGO [63].

B. Scintillation light-yield estimation

Due to the small size of samples, the measurement and determination of $Y_{lf,e}$ is more complicated than that for more typical larger samples. Escape peaks are enhanced while total absorption peaks are reduced under such circumstances. To correctly match absorbed energy with peaks observed in the spectra, the spectra of deposited energy are simulated by MCNP 6.2; see an example of the ^{109}Cd spectrum in Fig. S6 within the Supplemental Material [79]. ^{109}Cd emits γ photons with an energy of 88.04 keV and radiation yield of 3.61%, as well as several x-ray photons (Ag characteristic radiation), most notably, 21.99 keV (29.5%), 22.16 keV (55.7%), 24.91 keV (4.76%), 24.94 keV (9.2%), and 25.46 keV (2.3%) [64]. Simulation reveals an expected result that the measured spectrum should be dominated by one peak (21.99 and 22.16 keV), accompanied by a second peak (24.91, 24.94, and 25.46 keV). The 88.04-keV peak, which is otherwise easily found in the spectra of larger samples, should be at least 300 times smaller and its observability is questionable; see also Fig. S6 within the Supplemental Material [79]. Similarly, the Lu $K\alpha$ escape peak at 68.5 keV (122.1–53.7 keV) is quite intense in the ^{57}Co spectra.

Despite all the difficulties, estimated scintillation light-yield values are consistent with each other and the RL intensity as well, see Table I. The KLuS$_2$:Pr 0.5% sample exhibits $Y_{lf,e}$ approximately 50% higher than that of the KLuS$_2$:Pr 0.05% sample, which corresponds reasonably well with the steady-state values of RL spectra integrals.

In the case of Ce^{3+}-doped KLuS$_2$ (0.5% Ce), the $Y_{lf,e}$ value using ^{57}Co is determined to be 23 800 ph/MeV, bearing in mind that no significant Ce^{3+} $5d \rightarrow 4f$ luminescence quenching is observed around room temperature [26]. A typical amplitude spectrum of ^{109}Cd measured for the KLuS$_2$:Pr 0.5% sample can be seen in Fig. S7 within the Supplemental Material [79]. FWHM values are determined with significantly lower precision and reliability due to peak overlaps (namely, for ^{129}I and ^{57}Co), bad counting statistics (namely, ^{57}Co, due to low detection efficiency), and very low signals (namely, ^{55}Fe); therefore, we present only the FWHM values for ^{109}Cd: (110 ± 20)% (0.5% Pr) and (150 ± 30)% (0.05% Pr). Y_{lf} (^{55}Fe)/Y_{lf} (^{57}Co) = 0.89 for the KLuS$_2$:Pr 0.05% sample, which indicates a certain nonproportionality. Unfortunately, this nonproportionality is determined with very limited precision due to the sample thickness as well.

The knowledge of scintillation decay and $Y_{lf,e}$ values of KLuS$_2$:Pr^{3+} 0.5% can be used to determine the number of scintillation photons produced within the first nanosecond of the scintillation pulse (at ~22 keV). We also compare this value to the state-of-the-art material for fast timing: LYSO:Ce, Ca (see, for example, Ref. [61]). This is a crucially important parameter for the application potential of a given material in fast-timing fields (for example, time-of-flight positron emission tomography). Details of the calculation can be found in the Supplemental Material [79] text on "The calculation of the number of photons released by KLuS$_2$:Pr^{3+} 0.5%." The scintillation decay (under polychromatic x-ray excitation from the W tube at 40 kV) and scintillation light yield of a commercially available LYSO:Ce, Ca sample are measured using identical experimental setups and procedures to those used for KLuS$_2$:Pr 0.5%; therefore, these quantities for the two materials can be compared. The scintillation decay of the commercially available LYSO:Ce, Ca sample is displayed in Fig. S8 within the Supplemental Material [79]. The nonproportionality of the scintillation response must be, however, considered [62]; see also the Supplemental Material [79] for details in the text on "The calculation of the number of photons released by KLuS$_2$:Pr^{3+} 0.5%." As a result, it can be stated that, in the case of the LYSO:Ce, Ca reference sample, 670 photons (per MeV) are emitted by the sample in the first nanosecond, while, in the case of KLuS$_2$:Pr^{3+} 0.5%, 1080–1680 photons (per MeV) are released. These

TABLE I. Light-yield estimates for KLuS$_2$:Pr samples.

Peak origin	Energy (keV)	$Y_{l,e}$KLuS$_2$:Pr 0.5% (ph/MeV)	$Y_{l,e}$KLuS$_2$:Pr 0.05% (ph/MeV)
^{55}Fe	5.9	6380 ± 270	Not determined
^{109}Cd	22.1	7160 ± 220	4570 ± 140
^{129}I	29.7	6920 ± 210	4660 ± 140
^{57}Co (escape peak of Lu $K\alpha$)	68.5	7000 ± 210	Not determined
^{57}Co	122.1	7140 ± 210	Not determined

two values represent the limit cases of extrapolation of the scintillation decay of KLuS$_2$:Pr^{3+} 0.5% to the 1-µs time window used for scintillation light-yield measurements; the most probable value lies within this interval. The scintillation decay (E_x = 40 kV x-ray) of KLuS$_2$:Pr^{3+} 0.5% and extrapolation of the decay to 1 µs after t_0 with two limiting cases can be seen in Fig. S9 within the Supplemental Material [79]. Therefore, there is 1.6–2.5 times more scintillation light released by KLuS$_2$:Pr^{3+} 0.5% within the first nanosecond when compared to LYSO:Ce, Ca commercial standard; this makes KLuS$_2$:Pr^{3+} 0.5% superior from this application point of view. Very often, in R&D on ultrafast scintillators, only the scintillation rise time is considered for comparing two materials [42–44], but, in this particular case, no measurable rise time is observed for KLuS$_2$:Pr^{3+} 0.5% [see Fig. 4(b)] or LYSO:Ce, Ca (see Fig. S8 within the Supplemental Material [79]) in the given time window of 1 µs.

Furthermore, considering the overall radioluminescence efficiency of KLuS$_2$:Pr^{3+} 0.5% to be 320% that of BGO [see Fig. 3(a)], it should lead to a scintillation LY for KLuS$_2$:Pr^{3+} 0.5% of about 25 000 ph/MeV [63]. However, the value of only $Y_{l,f,e}$ = 7160 ph/MeV (see above) indicates that a significant amount of light is not emitted as part of the fast scintillation component, which corresponds well with the presence of afterglow, see Fig. 5. From this point of view, as already stated above, there is huge room for improvement.

C. Photoluminescence measurements

PL (a) and PLE (b) spectra of KLuS$_2$:Pr 0.05% recorded at 77 K for various excitation and emission wavelengths are shown in Fig. 6. The PL spectra, both under the band

gap and $4f \rightarrow 5d$ Pr^{3+} absorption-band excitation, are dominated by well-resolved emission bands corresponding to the Pr^{3+} $5d \rightarrow 4f$ transitions, which are in good agreement with the RL spectra, see Fig. 3. Under these excitation wavelengths, the intensity of the $^3P_0 \rightarrow {}^3H_4$ transition at 491 nm is negligible. PLE spectra measured for various emission wavelengths are composed of several spectral features, see Fig. 6(b). At the lowest-energy side, the Pr^{3+} $4f \rightarrow 5d$ absorption lines are visible in the 310–360-nm spectral region. The absorption-band gap is located at 280 nm, matching well with the previously reported low-temperature value [26]. Taking the lowest-absorption band of Pr^{3+} at 342 nm (77 K) and the $4f\,^15d^1 \rightarrow {}^3H_4$ emission band at 377 nm (77 K) yields the Stokes shift of 0.337 eV.

Figure 7 shows the photoluminescence decay curves connected to the Pr^{3+} $4f\,^15d^1 \rightarrow {}^3H_4$ emission of KLuS$_2$:Pr 0.05% (a) (λ_{ex} = 339 nm, λ_{em} = 380 nm) and KLuS$_2$:Pr 0.5% (b) (λ_{ex} = 339 nm, λ_{em} = 378 nm) measured at 77 K. Corresponding radiative decay times are 17.4 and 16.6 ns for 0.05% and 0.5% samples, respectively, with the hint of a much slower component, the origin of which is not clear. These values are in good agreement with the expected values of the fully allowed Pr^{3+} $5d \rightarrow 4f$ transition. For comparison, the radiative decay times of well-known scintillators doped with Pr^{3+} are 19.5 ns in Lu$_3$Al$_5$O$_{12}$:Pr^{3+} [65], 18.3 ns in LaPS:Pr^{3+} [66], or even 7.5 ns in YAlO$_3$ [60]. Other hosts are under consideration in Ref. [60], such as LiYF$_4$ (τ = 18.1 ns), LuPO$_4$ (τ = 15.4 ns), or LaBO$_3$ (τ = 12.7 ns) [60, and references therein]. PL and PLE spectra, with the onset of the multiplication of electronic excitation ($>2E_g$) below 150 nm [67], recorded at DESY for the vacuum UV spectra, are given in the Supplemental Material [79]. Figures S10(a) shows the PLE spectrum for the 380-nm emission and

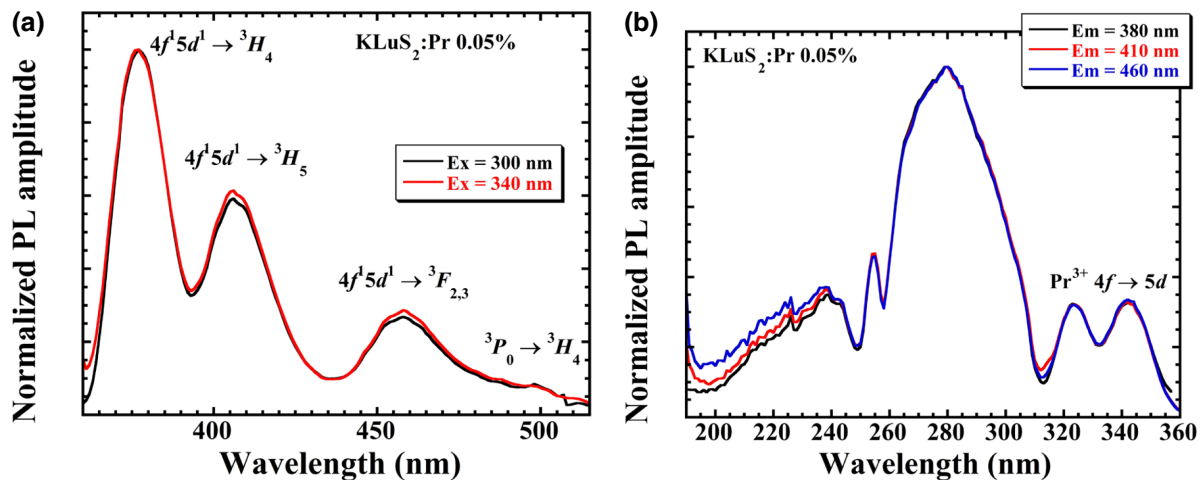FIG. 6.   (a) 77-K PL spectra (λ_{ex} = 300 nm, λ_{ex} = 340 nm) and (b) PLE spectra (λ_{em} = 380 nm, λ_{em} = 410 nm, λ_{em} = 460 nm) of KLuS$_2$:Pr 0.05% for various excitation and emission wavelengths (see legends).

(a)

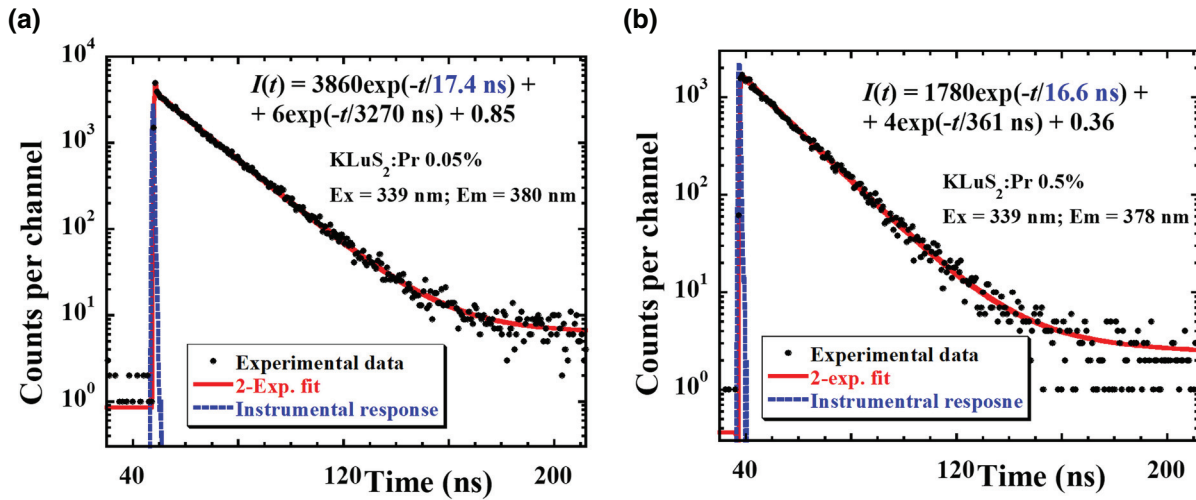$I(t) = 3860\exp(-t/17.4\text{ ns}) +$
$+ 6\exp(-t/3270\text{ ns}) + 0.85$

KLuS$_2$:Pr 0.05%

Ex = 339 nm; Em = 380 nm

- Experimental data
- 2-Exp. fit
- Instrumental response

(b)

$I(t) = 1780\exp(-t/16.6\text{ ns}) +$
$+ 4\exp(-t/361\text{ ns}) + 0.36$

KLuS$_2$:Pr 0.5%

Ex = 339 nm; Em = 378 nm

- Experimental data
- 2-exp. fit
- Instrumental resposne

FIG. 7. (a) 77-K PL decay curve connected to the Pr^{3+} $5d \to 4f$ transition ($\lambda_{ex} = 339$ nm, $\lambda_{em} = 380$ nm) of KLuS$_2$:Pr 0.05% (b) and Pr^{3+} $5d \to 4f$ transition ($\lambda_{ex} = 339$ nm, $\lambda_{em} = 378$ nm) of KLuS$_2$:Pr 0.5%. Solid line is a convolution of the instrumental response and function $I(t)$ in the figure.

Fig. S10(b) within the Supplemental Material [79] shows the PL spectrum under 50-nm excitation.

V. PHENOMENOLOGICAL MODELING

To investigate the temperature stability of the Pr^{3+} $5d \to 4f$ luminescence in the KLuS$_2$ host, we perform the temperature-dependent measurement of the PL spectra integrals ($\lambda_{ex} = 340$ nm, integrated in the Pr^{3+} $5d \to 4f$ region), see Figs. 8(a) and 8(b), and of the Pr^{3+} $4f^1 5d^1 \to {}^3H_4$ decay times ($\lambda_{ex} = 339$ nm, $\lambda_{em} = 380$ nm), see Figs. 8(c) and 8(d), for two different Pr concentrations (0.5%, 0.05%). The PL spectra integral of the 0.5% sample is constant in the 77–177-K temperature region. It starts to decrease at higher temperatures and reaches 4% of its low-temperature limit at 317 K [Fig. 8(a)], while that of 0.05% Pr starts to decrease mildly already at 137 K and reaches 11% of its low-temperature limit at 300 K [Fig. 8(b)]. The PL decay times, for both Pr^{3+} concentrations, are constant at least up to 157 K and start to decrease with rising temperature. The low-temperature limits, which are usually referred to as radiative lifetimes, are 16.6 and 17.4 ns for the 0.5% and 0.05% samples, respectively, while room-temperature values reach 0.7 and 2.1 ns, respectively.

A phenomenological model in the form outlined in Eqs. (4)–(6) is fitted to the PL-decay-time temperature dependence and PL-spectra-integral temperature dependence. The former dependence can be described by simple barrier quenching:

$$\frac{1}{\tau}(T) = \frac{1}{\tau_r} + K_x e^{-(E_x/kT)}, \qquad (4)$$

where τ, τ_r, K_x, E_x, k, and T represent the observed decay time at temperature T, the low-temperature limit of the PL decay time (radiative decay time), the frequency factor of the nonradiative escaping channel, its energy barrier height, the Boltzmann constant, and the absolute temperature, respectively. The time evolution of the population, N, of the emitting-center excited state is given by the rate equation:

$$dN(t)/dt = -\left(\frac{1}{\tau}\right)N(t), \qquad (5)$$

and hence, the temperature dependence of the integrated PL intensity is given as

$$I(T) = N_0 \frac{1}{\tau_r}\tau(T), \qquad (6)$$

where N_0 stands for an initial population of the excited state of the emitting center and is set to 1 in the calculation [solid curves in Figs. 8(a) and 8(b)]. For $\tau(T)$, Eq. (4) and values from the PL-decay-time temperature-dependence fit [Figs. 8(c) and 8(d)] are used. A satisfactory fit to the experimental data of PL spectra integrals and PL decay times as a function of temperature can be obtained with the following parameters: $\tau_r = 16.8 \times 10^{-9}$ s, $K_x = 1.8 \times 10^{12}$ s^{-1}, and $E_x = 200$ meV for the 0.5% sample; and $\tau_r = 17.4 \times 10^{-9}$ s, $K_x = 9.5 \times 10^{11}$ s^{-1}, and $E_x = 200$ meV for the 0.05% sample. To determine whether the intensity and decay time decrease is due to luminescence thermal quenching or thermally induced ionization of the Pr^{3+} $5d$ excited state, an independent analysis of the thermoluminescence and delayed recombination measurements would have to be conducted (see, for
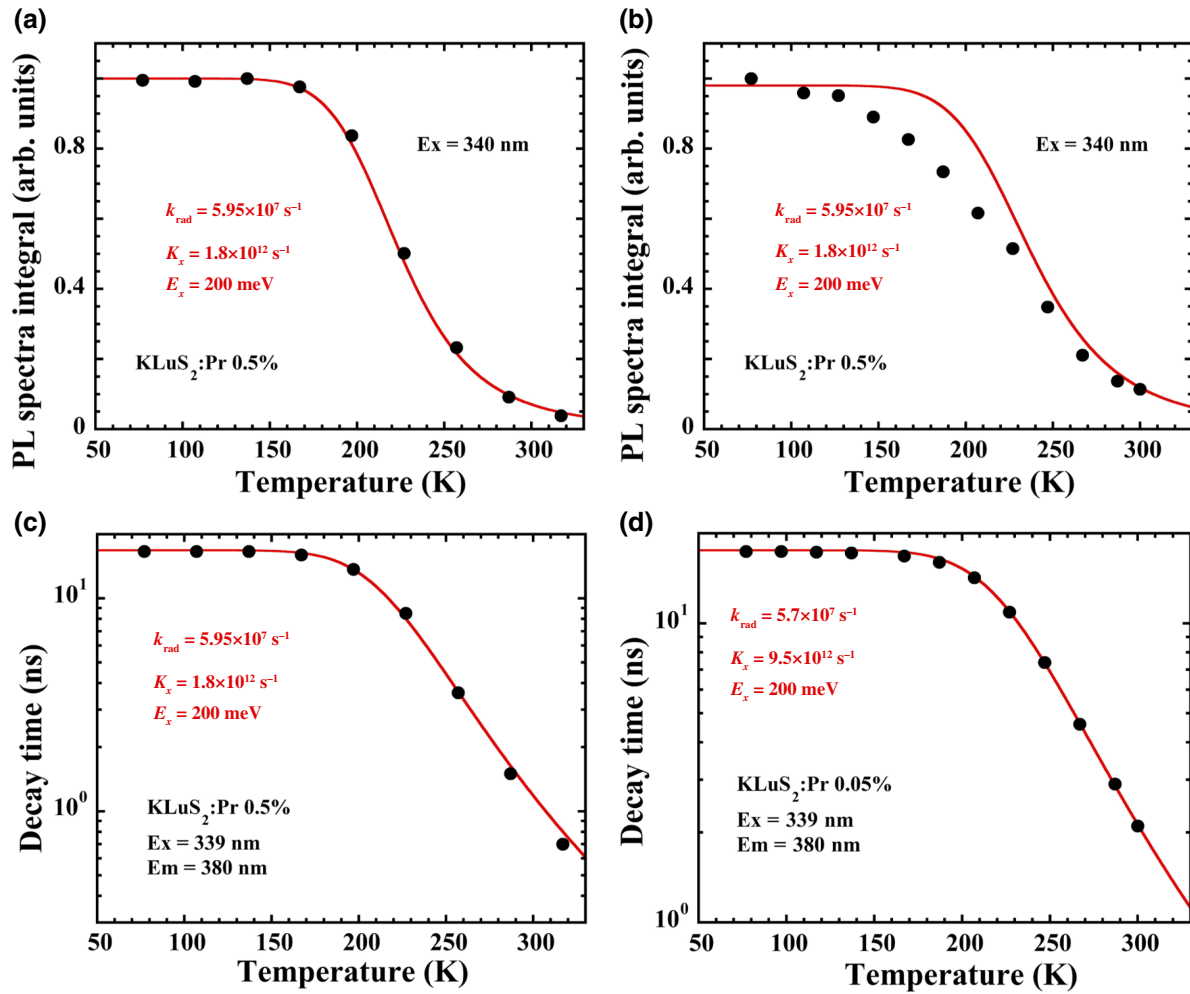
FIG. 8. Temperature dependence of PL spectra integrals ($\lambda_{ex} = 340$ nm) of (a) KLuS$_2$:Pr^{3+} 0.5%, PL integration range 360–435 nm; and (b) KLuS$_2$:Pr^{3+} 0.05%, PL integration range 360–490 nm; and temperature dependence of PL decay times connected to the Pr^{3+} $5d \rightarrow 4f$ transition ($\lambda_{ex} = 339$ nm, $\lambda_{em} = 380$ nm) of (c) KLuS$_2$:Pr^{3+} 0.5% and (d) KLuS$_2$:Pr^{3+} 0.05%.

example, Ref. [68]); this is beyond the scope of the present work. To explain the noticeable discrepancy between the experimental values of the PL spectra integral of KLuS$_2$:Pr 0.05% and the fit, see Fig. 8(b), the EPR technique is applied to the KLuS$_2$:Pr 0.05% sample.

VI. CHARGE-TRAPPING PROCESSES IN KLuS$_2$:Pr 0.05% BY EPR

It is commonly known that charge-trapping processes can be effectively studied by applying the EPR technique [69] to the x-ray-irradiated sample. The smaller the particle size, the larger the irradiated volume of a single powder particle, and consequently, the larger number of charge-trapping centers that can be activated. It was recently proved for Li$_2$MoO$_4$ single crystals [69]. In this case, the charge-trapping phenomena are investigated only for the KLuS$_2$:Pr 0.05% sample, particularly for the fraction of smaller crystals, as grinding KLuS$_2$ platelets into powder can lead to oxidation to Lu$_2$O$_2$S [47].

No signals are detected in the EPR spectra of the KLuS$_2$:Pr 0.05% sample prior to x-ray irradiation, whereas, after exposure to x-rays at 60 K, some resonances become visible, see Fig. 9.

Signals QH1-4 originate from the quartz sample holder, which is inevitably irradiated along with the sample itself, as proven by the spectrum measured for the empty holder [Fig. 9(a)]. It is a well-known fact that charge trapping occurs in x-ray-irradiated quartz (see, e.g., Refs. [71,72], and references therein).

Signals 1–4 originate from the KLuS$_2$:Pr 0.05% sample. This leads to the conclusion that these signals are the result of charge trapping evoked by x-rays and the creation of a paramagnetic particle(s) from the nonparamagnetic one(s). There are four clearly distinguished contributions, which are designated as 1–4 [Fig. 9(a)]. Signals 1–4 have approximately the same intensity in the x-ray irradiated but not annealed KLuS$_2$:Pr 0.05% sample. To study the thermal stability of the created charge-trapping centers, the
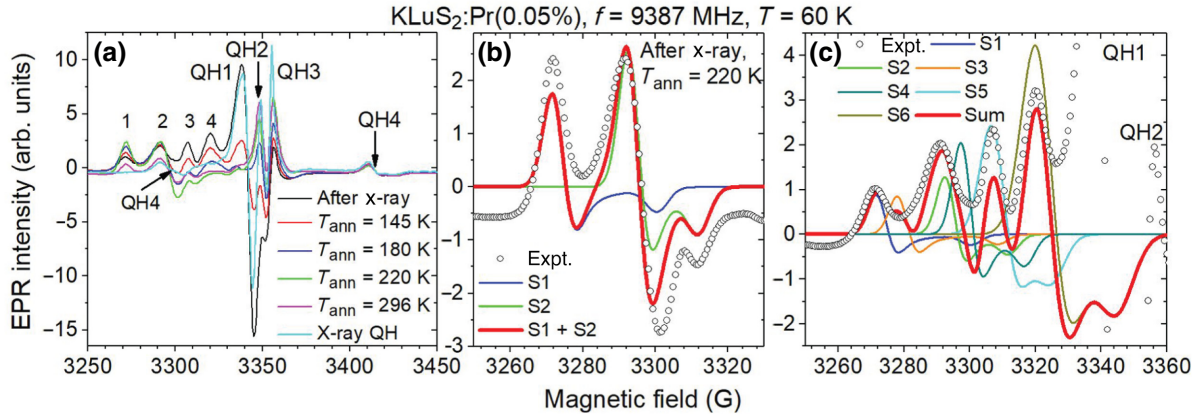
FIG. 9.   (a) EPR spectra measured at 60 K immediately after x-ray irradiation and after annealing at certain temperatures (T_{ann} in the legend) for the KLuS$_2$:Pr 0.05% sample. Numbers 1–4 indicate the specific transitions occurring after irradiation. Their evolution under the elevated annealing temperature can be studied. (b) Approximation of experimental signals 1 and 2 in the KLuS$_2$:Pr 0.05% sample irradiated and annealed at $T_{ann} = 220$ K with the calculated ones. (c) Approximation of signals 1–4 in the irradiated KLuS$_2$:Pr 0.05% sample. QH1–4 indicate the signals originating from the quartz sample holder.

pulse annealing method is used. The sample is annealed stepwise in the cryostat cycle by cycle at the elevated annealing temperature (prompt heating and cooling) for 4 min (the time sufficient for good thermalization of the sample), whereas the EPR spectrum is measured at a constant temperature of 60 K each time. The intensity of signals 3 and 4 drops, whereas the intensity of signals 1 and 2 rise upon increasing the annealing temperature [within the 145–220-K range, Fig. 9(a)]. Since EPR intensity is directly proportional to the paramagnetic particle concentration [73], the redistribution of trapped charges between the origins of signals 3,4 and 1,2 can be expected in this case. The intensities of signals 1 and 2 exhibit different dependences on the annealing temperature, as seen in Fig. 9(a). Based on these observations, one may conclude that they have different origins, rather than being the components of the same anisotropic signal [73]. The intensity of signals 1 and 2 reaches a maximum after annealing at 220 K. Signals 3 and 4 no longer exist under these conditions [Fig. 9(b)]. Further increase of the annealing temperature to 296 K leads to about twofold decrease of the intensity of signals 1 and 2, compared to those at 220 K. Therefore, resonances 1 and 2 can be unambiguously analyzed after annealing of the sample at 220 K. The corresponding spectrum is shown in Fig. 9(b) in more detail. Since no other resonances are observed, the electron spin of the paramagnetic particle producing these signals is $S = 1/2$ in both cases. The following spin-Hamiltonian (with only the Zeeman term [73]) is used to approximate overlapping signals 1 and 2 as the total signal [S1 and S2, respectively, and S1 + S2 in Fig. 9(b)]:

$$\hat{\mathbf{H}} = \beta \hat{\mathbf{S}} \hat{\mathbf{g}} H, \qquad (7)$$

where β is the Bohr magneton, $\hat{\mathbf{S}}$ is the electron vector spin operator, $\hat{\mathbf{g}}$ is the g tensor, and **H** is the resonance magnetic field. The fit is reasonably good. Slight disagreement between experimental and calculated spectra is explained by the overlap of signals 1 and 2 with the QH4 signal [Figs. 9(a) and 9(b)]. The g-tensor principal values determined from the fit are listed in Table II.
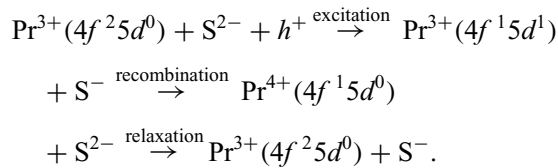
The g tensors of signals 1 and 2 are axial. This is in a good agreement with the hexagonal symmetry of the KLuS$_2$ single crystal [34–37]. Their principal values are larger than 2.0023, which is the value of a free electron. This is a typical situation for a more than half-filled outer shell. Moreover, approximately the same values are obtained for the O$-$ defects in oxides [70,74,75]. Therefore, referring to the chemical formula of the sulfide, the only possibility is the creation of the S$-$ ($3p^5$) centers (S1 and S2 producing signals 1 and 2, respectively) by hole trapping: S^{2-} + h^+ $\xrightarrow{\text{x-ray}}$ S$^-$. $\hat{\mathbf{g}}_{S1} > \hat{\mathbf{g}}_{S2}$ (Table II). Therefore, the S$-$ center in each case appears at different local crystal fields, i.e., different local surroundings, and different lattice positions [73]. Since there is only one crystallographic anion site in the KLuS$_2$ lattice, both $\hat{\mathbf{g}}_{S1,S2}$ are axial and the thermal stability of the S1 and S2 centers is high (they survive annealing at 296 K), and both are expected to appear at regular S sites, most probably,

TABLE II.   Principal g tensor values [Eq. (7)].

Signal	$\hat{\mathbf{g}}$		
	g_1	g_2	g_3
S1	2.049	2.049	2.032
S2	2.036	2.036	2.025
S3	2.027	2.027	2.017
S4	2.019	2.019	2.005
S5	2.045	2.045	2.027
S6	2.033	2.033	2.022

perturbed along the trigonal axis of symmetry (*c* axis). Now, knowing $\hat{\mathbf{g}}_{S1,S2}$, the spectrum obtained immediately after x-ray irradiation can be decomposed into its components using Eq. (7) [Fig. 9(c)]. In fact, it is possible to resolve four contributions overlapping with signals 1 and 2 and creating signals 3 and 4 [S5,6 and S3,4, respectively, in Fig. 9(c)]. The corresponding $\hat{\mathbf{g}}_{S3 - S6}$ *g* tensors are found by analogy with S1,2 [Eq. (7)] and listed in Table II as well. The calculated spectrum is in good agreement with the experimental one. Since the $\hat{\mathbf{g}}_{S5,S6}$ principal values are close to those of $\hat{\mathbf{g}}_{S1,S2}$, one may infer that the S5,6 centers are similar to the perturbed S1,2, but have lower thermal stability [not observed in the spectrum measured after annealing at 220 K, as seen in Fig. 9(b)]. $\hat{\mathbf{g}}_{S3,S4}$ are axial. The corresponding principal values are larger than 2.0023, the free electron value, and therefore, by analogy with the S1,2 centers, they are expected to originate from S− defects as well. They disappear after annealing at 220 K. This thermal stability is rather high to conclude the existence of the self-trapping processes [73,74]. Therefore, there must be quite a few defects (impurities, intentional like Pr, or accidental ones, or imperfections like cation vacancies, antisites, etc.) perturbing the local surroundings of S−, most probably along the *c* axis to preserve axiality. It should be mentioned that no signals like the ones shown in Fig. 9 are observed for undoped KLuS$_2$. This leads to the conclusion that the S1–6 signals appear only due to the presence of Pr^{3+}. This is also confirmed by the relatively high thermal stability of the mentioned signals (induced by x-ray irradiation, they survive even after annealing at 220–296 K). Typically, the self-trapped charges (not influenced by any imperfection nearby) have much lower thermal stability (below 150 K) [76].

Note that the S3–6 hole-trapping centers disappear in the 77–220-K range, whereas S1,2 become stronger. This might explain the deviation of the fitting curve calculated in the framework of the phenomenological model from the experimental temperature dependence of the integral PL intensity in Fig. 8(b). One may conclude that hole trapping, in turn, may participate in the Pr^{3+} $4f\,^1 5d^1 \rightarrow 4f\,^2 5d^0$ luminescence processes. The electron from the excited Pr^{3+} $5d^1$ state can move to the S− defect, temporarily creating S^{2-}, subsequently returning to the Pr^{3+} ground state nonradiatively. The whole process of excitation and nonradiative relaxation can be described by the following mechanism for the 77–220-K temperature range:

$$\mathrm{Pr}^{3+}(4f\,^2 5d^0) + \mathrm{S}^{2-} + h^+ \overset{\mathrm{excitation}}{\rightarrow} \mathrm{Pr}^{3+}(4f\,^1 5d^1)$$

$$+ \mathrm{S}^- \overset{\mathrm{recombination}}{\rightarrow} \mathrm{Pr}^{4+}(4f\,^1 5d^0)$$

$$+ \mathrm{S}^{2-} \overset{\mathrm{relaxation}}{\rightarrow} \mathrm{Pr}^{3+}(4f\,^2 5d^0) + \mathrm{S}^-.$$

A similar mechanism was recently described for the Eu^{2+}-F$^+$ center in Y$_3$Al$_5$O$_{12}$ [77]. Alternatively, the mentioned

deviation of the fitting curve [Fig. 8(b)] can be explained by temperature dependence of $4f \rightarrow 5d^1$ absorption amplitude, as it is a well-known phenomenon in Ce^{3+}-doped materials [78]. However, a well-grounded explanation would require an independent study and will be the subject of further investigation.

No EPR signals connected to Pr^{3+} or Pr^{4+} are detected in the KLuS$_2$:Pr^{3+} 0.05% sample. However, the EPR spectra typical for Er^{3+} and Yb^{3+} are observed, and their properties are discussed further in the Supplemental Material [79], particularly Fig. S11 and the corresponding text.

VII. CONCLUSIONS

Here, we present the Pr^{3+}-doped KLuS$_2$ single-crystalline material as potentially interesting superfast x-ray phosphor. By an inorganic reaction in an electric resistance furnace, we prepare the optically transparent colorless single-crystal samples about 0.1 mm thick with a cross-section area up to a few square mm, consisting of the single KLuS$_2$ phase. The room-temperature absorption spectrum shows the KLuS$_2$ band edge at around 300 nm and the Pr^{3+} $4f$ -$5d$ absorption band peaking at 347 nm. Both x-ray and photoluminescence excitation provide the broad Pr^{3+} $5d$-$4f$ emission peaking in the 380–460-nm spectral range and characteristic Pr^{3+} $4f$ -$4f$ emission peaks in the visible part of the spectrum. The RL spectra integrals for KLuS$_2$:Pr 0.05% and KLuS$_2$:Pr 0.5% provide 190% and 320% of the BGO integral at room temperature, respectively. The afterglow curve of KLuS$_2$:Pr 0.5% shows a drop of intensity down to 7% after 10 ms following x-ray excitation cutoff and a further mild decrease at longer times. Both the room-temperature photoluminescence and scintillation decay time of the Pr^{3+} center feature a leading component of about 1–2 ns with slower components of lower amplitudes. At low temperature, a Stokes-shift value of 340 meV can be evaluated from the photoluminescence excitation and emission spectra, with a corresponding photoluminescence decay time of 17.4 ns (0.05% Pr) and 16.6 ns (0.5% Pr). The room-temperature scintillation light yield of KLuS$_2$:Pr is estimated to be at least 7160 ph/MeV for the 0.5% Pr sample and 4570 ph/MeV for the 0.05% Pr sample by using 22.1-keV x-ray radiation from the ^{109}Cd radionuclide. It is therefore comparable to the scintillation light yield of Bi$_4$Ge$_3$O$_{12}$ single crystals commonly used in various applications. The ratio of light yields measured by ^{55}Fe and ^{57}Co is 0.89 for the KLuS$_2$:Pr 0.05% sample, which points to a rather small nonproportionality. A phenomenological model is employed to describe the Pr^{3+} excited-state dynamics and explain the nanosecond decay-time reduction with increasing temperature. The parameters of the best fitting of Eqs. (4) and (6) to experimental data are $\tau_r = 16.8 \times 10^{-9}$ s, $K_x = 1.8 \times 10^{12}$ s^{-1}, and $E_x = 200$ meV for the 0.5% sample; and $\tau_r = 17.4 \times 10^{-9}$ s, $K_x = 9.5 \times 10^{11}$ s^{-1}, and

$E_x = 200$ meV for the 0.05% samples. Several defects perturbing the local surroundings of the S− center are characterized by EPR. The observed disagreement between the observed temperature dependence of the emission-spectra integral of KLuS$_2$:Pr 0.05% and the applied model can be explained by hole trapping participating in the Pr^{3+} $4f^{1}5d^{1} \rightarrow 4f^{2}5d^{0}$ luminescence processes.

An elevated effective atomic number ($Z_{eff} = 59$) and density ($\rho = 4.69$ g cm^{-3}); a scintillation light yield estimated to be at least 7200 ph/MeV with a leading scintillation decay time under 1 ns; efficient energy transfer from the host to Pr^{3+} centers; and a lower band gap, relative to oxide-based materials, are intrinsic advantages of Pr^{3+}-doped KLuS$_2$. Furthermore, the number of photons emitted in the first nanosecond of the scintillation response is considerably higher (1.6–2.5 times) than that in the commercial LYSO:Ce, Ca scintillator, which shows the potential of Pr^{3+}-doped KLuS$_2$ for fast-timing scintillator applications.

ACKNOWLEDGMENT

[1] M. Nikl and A. Yoshikawa, Recent R&D trends in inorganic single-crystal scintillator materials for radiation detection, Adv. Opt. Mater. **3**, 463 (2015).

[2] P. T. Dickens, D. T. Haven, S. Friedrich, and K. G. Lynn, Scintillation properties and increased vacancy formation in cerium and calcium co-doped yttrium aluminum garnet, J. Cryst. Growth **507**, 16 (2019).

[3] E. Gordienko, A. Fedorov, E. Radiuk, V. Mechinsky, G. Dosovitskiy, E. Vashchenkova, D. Kuznetsova, V. Retivov, A. Dosovitskiy, M. Korjik, and R. Sandu, Synthesis of crystalline Ce-activated garnet phosphor powders and technique to characterize their scintillation light yield, Opt. Mater. **78**, 312 (2018).

[4] M. V. Derdzyan, K. L. Hovhannesyan, A. V. Yeganyan, R. V. Sargsyan, A. Novikov, A. G. Petrosyan, and Ch. Dujardin, Dissimilar behavior of YAG:Ce and LuAG:Ce scintillator garnets regarding Li^{+} co-doping, CrystEngComm **20**, 1520 (2018).

[5] D. Bucevac and V. Krstic, The effect of SiC addition on photoluminescence of YAG:Ce phosphor for white LED, J. Eur. Ceram. Soc. **38**, 5519 (2018).

[6] M. Borlaf, M. Frankowska, W. W. Kubiak, and T. Graule, Ce^{3+} and Eu^{3+} emissions in YAG via a core-shell strategy for warm white LED lighting, J. Sol-Gel Sci. Technol. **86**, 1 (2018).

[7] H. R. Abd, Z. Hassan, M. N. Ahmed, M. A. Almessiere, A. F. Omar, F. H. Alsultany, A. F. Sabah, and U. S. Osman, Effect of annealing time of YAG:Ce^{3+} phosphor on white light chromaticity values, J. Electron. Mater. **47**, 1638 (2018).

[8] R. Boulesteix, L. Bonnet, A. Maitre, L. Chretien, and C. Sallé, Silica reactivity during reaction-sintering of Nd:YAG transparent ceramics, J. Am. Ceram. Soc. **100**, 945 (2017).

[9] V. Lupei, A. Lupei, C. Gheorghe, and A. Ikesue, Emission sensitization processes involving Nd^{3+} in YAG, J. Lumin. **170**, 594 (2016).

[10] J. Azkargorta, I. Iparraguirre, M. Barredo-Zuriarrain, S. García-Revilla, R. Balda, and J. Fernández, Random laser action in Nd:YAG crystal powder, Materials **9**, 369 (2016).

[11] G. A. Bufetova, V. V. Kashin, S. Y. Rusanov, V. F. Seregin, and V. B. Tsvetkov, Measurement of the refractive index of an Er^{3}:YAG crystal melt, J. Appl. Phys. **127**, 035104 (2020).

[12] S. Bigotta, L. Galecki, A. Katz, J. B. Hmler, S. Lemonnier, E. Barraud, A. Leriche, and M. Eichhorn, Resonantly pumped eye-safe Er^{3+}:YAG SPS-HIP ceramic laser, Opt. Express **26**, 3435 (2018).

[13] M. Chaika, O. Vovk, G. Mancardi, R. Tomala, and W. Strek, Dynamics of Yb^{2+} to Yb^{3+} ion valence transformations in Yb:YAG ceramics used for high-power lasers, Opt. Mater. **101**, 109774 (2020).

[14] A. Pirri, G. Toci, J. Li, Y. Feng, T. Xie, Z. Yang, B. Patrizi, and M. Vannini, A comprehensive characterization of a 10 at.% Yb:YSAG laser ceramic sample, Materials **11**, 837 (2018).

[15] J. Šulc, R. Švejkar, M. Fibrich, H. Jelínková, L. Havlák, V. Jarý, M. Ledinský, M. Nikl, J. Bárta, M. Buryi, R. Lorenzi, F. Cova, and A. Vedda, Infrared spectroscopic properties of low-phonon lanthanide-doped KLuS$_2$ crystals, J. Lumin. **211**, 100 (2019).

[16] M. Ebrahim-Zadeh, and I. T. Sorokina, in *Part of the NATO Science for Peace and Security Series B: Physics and Biophysics book series (NAPSB)* (Springer, 2008), p. 3.

[17] J. Ganem, J. Crawford, P. Schmidt, N. W. Jenkins, and S. R. Bowman, Thulium cross-relaxation in a low phonon energy crystalline host, Phys. Rev. B **66**, 28012 (2002).

[18] J. Ganem and S. R. Bowman, Use of thulium-sensitized rare earth-doped low phonon energy crystalline hosts for IR sources, Nanoscale Res. Lett. **8**, 455 (2013).

[19] V. Jarý, L. Havlák, J. Bárta, E. Mihóková, and M. Nikl, Optical properties of Eu^{2+}-doped KLuS$_2$ phosphor, Chem. Phys. Lett. **574**, 61 (2013).

[20] V. Laguta, M. Buryi, L. Havlák, J. Bárta, V. Jarý, and M. Nikl, Stabilization of Eu^{2+} in KLuS$_2$ crystalline host: An EPR and optical study, Phys. Status Solidi RRL **8**, 801 (2014).

[21] V. Jarý, L. Havlák, J. Bárta, M. Buryi, E. Mihóková, M. Rejman, V. Laguta, and M. Nikl, Optical, structural and paramagnetic properties of Eu-doped ternary sulfides

ALnS$_2$ (A = Na, K, Rb; Ln = La, Gd, Lu, Y), Materials **8,** 6978 (2015).

[22] V. Jarý, L. Havlák, J. Bárta, M. Buryi, M. Rejman, M. Pokorný, Ch. Dujardin, G. Ledoux, and M. Nikl, Variability of Eu^{2+} Emission features in multicomponent alkali-metal-rare-earth sulfides, ECS J. Solid State Sci. Technol. **9,** 016007 (2020).

[23] V. Jarý, L. Havlák, J. Bárta, M. Rejman, A. Bystřický, Ch. Dujardin, G. Ledoux, and M. Nikl, Circadian light source based on K$_x$Na$_{1-x}$LuS$_2$:Eu^{2+} phosphor, ECS J. Solid State Sci. Technol. **7,** R3182 (2018).

[24] L. Havlák, V. Jarý, J. Bárta, M. Buryi, M. Rejman, V. Laguta, and M. Nikl, Tunable Eu^{2+} emission in K$_x$Na$_{1-x}$LuS$_2$ phosphors for white LED application, Mater. Des. **106,** 363 (2016).

[25] L. Havlák, V. Jarý, M. Rejman, E. Mihóková, J. Bárta, and M. Nikl, Luminescence characteristics of doubly doped KLuS$_2$:Eu, RE (RE = Pr, Sm, Ce), Opt. Mater. **41,** 94 (2015).

[26] V. Jarý, L. Havlák, J. Bárta, E. Mihóková, P. Průša, and M. Nikl, Optical properties of Ce^{3+}-doped KLuS$_2$ phosphor, J. Lumin. **147,** 196 (2014).

[27] V. Jarý, L. Havlák, J. Bárta, E. Mihóková, M. Buryi, and M. Nikl, ALnS$_2$:RE (A = K, Rb; Ln = La, Gd, Lu, Y): New optical materials family, J. Lumin. **170,** 718 (2016).

[28] A. Allah, M. Halit, S. Saib, L. Azzouz, S. Maabed, M. Bouchenafa, and R. Ahuja, A comparative theoretical investigation of optoelectronic and mechanical properties of KYS$_2$ and KLaS$_2$, Mater. Sci. Semicond. Process. **113,** 105048 (2020).

[29] L. Azzouz, M. Halit, M. Sidoumou, Z. Charifi, A. Allal, M. Bouchenafa, and H. Baaziz, Electronic structure, elastic and optical properties of AEuS$_2$ (A = Na, K, Rb, and Cs) ternary sulfides: First-principles study, Phys. Status Solidi B **256,** 1900136 (2019).

[30] L. Azzouz, M. Halit, Z. Charifi, H. Baaziz, M. Rérat, H. Denawi, and Ch. F. Matta, Magnetic semiconductor properties of RbLnSe2 (Ln = Ce, Pr, Nd, Gd): A density functional study, J. Magn. Magn. Mater. **501,** 166448 (2020).

[31] L. Azzouz, M. Halit, A. Allal, S. Maabed, M. Bouchenafa, R. Ahmed, T. Seddik, A. Bouhemadou, and R. Khenata, Structural, electronic, optical and elastic properties of layered rhombohedral compounds ALaSe$_2$(A = K, Rb): Insights from an *ab initio* study, Int. J. Mod. Phys. B **33,** 1950084 (2019).

[32] L. Azzouz, M. Halit, M. Rérat, R. Khenata, A. K. Singh, M. M. Obeid, H. R. Jappor, and X. Wang, Structural, electronic and optical properties of ABTe$_2$ (A = Li, Na, K, Rb, Cs and B = Sc, Y, La): Insights from first-principles computations, J. Solid State Chem. **279,** 120954 (2019).

[33] L. Azzouz, M. Halit, Z. Charifi, and Ch. F. Matta, Tellurium doping and the structural, electronic, and optical properties of NaYS$_{2(1-x)}$Te$_{2x}$ alloys, ACS Omega **4,** 11320 (2019).

[34] J. Fábry, L. Havlák, M. Dušek, P. Vaněk, J. Drahokoupil, and K. Jurek, Structure determination of KLaS$_2$, KPrS$_2$, KEuS$_2$, KGdS$_2$, KLuS$_2$, KYS$_2$, RbYS$_2$, NaLaS$_2$ and crystal-chemical analysis of the group 1 and thallium(I) rare-earth sulfide series, Acta Crystallogr. B **70,** 360 (2014).

[35] L. Havlák, J. Fábry, M. Henriques, and M. Dušek, Structure determination of KScS$_2$, RbScS$_2$, and KLnS$_2$ (Ln = Nd, Sm, Tb, Dy, Ho, Er, Tm and Yb) and crystal-chemical discussion, Acta Crystallogr. C **71,** 623 (2015).

[36] J. Fábry, L. Havlák, M. Kučeráková, and M. Dušek, Redetermination of NaGdS$_2$, NaLuS$_2$ and NaYS$_2$, Acta Crystallogr. C **70,** 533 (2014).

[37] J. Fábry, L. Havlák, M. Henriques, M. Dušek, J. Rohlíček, M. Pasciak, M. Kopecký, and J. Kub, A new structural type in alkaline rare-earth sulfides MRES$_2$ and TIRES$_2$, Acta Crystallogr. A **71,** S311 (2015).

[38] J. S. Karp, S. Surti, M. E. Daube-Witherspoon, and G. Muehllehner, Benefit of time-of-flight in PET: Experimental and clinical results, J. Nucl. Med. **49,** 462 (2008).

[39] T. Jones and D. W. Townsend, History and future technical innovation in positron emission tomography, J. Med. Imaging **4,** 011013 (2017).

[40] S. Gundacker, F. Acerbi, E. Auffray, A. Ferri, A. Gola, M. V. Nemallapudi, G. Paternoster, C. Piemonte, and P. Lecoq, State of the art timing in TOF-PET detectors with LuAG, GAGG and L(Y)SO scintillators of various sizes coupled to FBK-SiPMs, J. Instrum. **11,** P08008 (2016).

[41] N. Aubry, *et al.*, EndoTOFPET-US: A novel multimodal tool for endoscopy and positron emission tomography, J. Instrum. **8,** C04002 (2013).

[42] S. Gundacker, R. M. Turtos, E. Auffray, M. Paganoni, and P. Lecoq, High-frequency SiPM readout advances measured coincidence time resolution limits in TOF-PET, Phys. Med. Biol. **64,** 055012 (2019).

[43] S. Gundacker, E. Auffray, K. Pauwels, and P. Lecoq, Measurement of intrinsic rise times for various L(Y)SO and LuAG scintillators with a general study of prompt photons to achieve 10 ps in TOF-PET, Phys. Med. Biol. **61,** 2802 (2016).

[44] P. Lecoq, *et al.*, Roadmap toward the 10 ps time-of-flight PET challenge, Phys. Med. Biol. **65,** 21RM01 (2020).

[45] M. Buryi, R. Král, V. Babin, J. Páterek, V. Vaněček, P. Veverka, M. Kohoutková, V. Laguta, M. Fasoli, I. Villa, F. Cova, A. Vedda, and M. Nikl, Trapping and recombination centers in cesium hafnium chloride single crystals: EPR and TSL study, J. Phys. Chem. C **123,** 19402 (2019).

[46] L. Havlák, J. Bárta, M. Buryi, V. Jarý, E. Mihóková, V. Laguta, P. Boháček, and M. Nikl, Eu^{2+} Stabilization in YAG structure: Optical and electron paramagnetic resonance study, J. Phys. Chem. C **120,** 21751 (2016).

[47] L. Havlák, V. Jarý, M. Nikl, P. Boháček, and J. Bárta, Preparation, luminescence and structural properties of RE-doped RbLaS$_2$ compounds, Acta Mater. **59,** 6219 (2011).

[48] M. G. Brik, V. Jarý, L. Havlák, J. Bárta, and M. Nikl, Ternary sulfides ALnS$_2$:Eu^{2+} (A = alkaline metal, Ln = rare-earth element) for lighting: Correlation between the host structure and Eu^{2+} emission maxima, Chem. Eng. J. **418,** 129380 (2021).

[49] V. Jarý, L. Havlák, J. Bárta, E. Mihóková, and M. Nikl, Luminescence and structural properties of RbGdS$_2$ compounds doped by rare earth elements, Opt. Mater. **35,** 1226 (2013).

[50] S. Gates-Rector and T. Blanton, The Powder Diffraction File: A quality materials characterization database, Powder Diffr. **34,** 352 (2019).

[51] M. Moszynski, M. Kapusta, M. Mayhugh, D. Wolski, and S. O. Flyck, Absolute light output of scintillators, IEEE Trans. Nucl. Sci. **44,** 1052 (1997).

[52] C. D'Ambrosio and H. Leutz, Hybrid photon detectors, Nucl. Inst. Meth. A **501,** 463 (2003).

[53] C. J. Werner, J. S. Bull, C. J. Solomon, F. B. Brown, G. W McKinney, M. E. Rising, D. A. Dixon, R. L. Martz, H. G. Hughes, L. J. Cox, A. J. Zukaitis, J. C. Armstrong, R. A. Forster, L. Casswell, MCNP6.2 Release Notes, Los Alamos National Laboratory (2018), report LA-UR-18-20808.

[54] V. Jarý, L. Havlák, J. Bárta, and M. Nikl, Preparation, luminescence and structural properties of rare-earth-doped $RbLuS_2$ compounds, Phys. Status Solidi RRL **6,** 95 (2012).

[55] A. M. Srivastava, U. Happek, and P. Schmidt, Luminescence of $LuCl_3$:Pr^{3+} under interconfigurational ($4f^2 \rightarrow 4f^1 5d^1$) and band gap excitations, Opt. Mater. **31,** 213 (2008).

[56] A. M. Srivastava, Identification of the $I^- \rightarrow Pr^{3+}$ charge transfer transition in the excitation spectrum of LuI_3:Pr^{3+}, Opt. Mater. **30,** 1567 (2008).

[57] M. Y. A. Yagoub, H. C. Swart, P. Bergman, and E. Coetsee, Enhanced Pr^{3+} photoluminescence by energy transfer in SrF_2 : Eu^{2+}, Pr^{3+} phosphor, AIP Adv. **6,** 025204 (2016).

[58] P. V. dos Santos, E. A. Gouveia, M. T. de Araujo, A. S. Gouveia-Neto, S. J. L. Ribeiro, and S. H. S. Benedicto, IR-visible upconversion and thermal effects in Pr^{3+}/Yb^{3+}-codoped Ga_2O_3:La_2S_3 chalcogenide glasses, J. Phys.: Condens. Matter **12,** 10003 (2000).

[59] W. T. Carnall, G. L. Goodmann, K. Rajnak, and R. S. Rana, A systematic analysis of the spectra of the lanthanides doped into single crystal LaF_3, J. Chem. Phys. **90,** 3443 (1989).

[60] A. Zych, M. de Lange, C. de Mello Donegá, and A. Meijerink, Analysis of the radiative lifetime of Pr^{3+} d-f emission, J. Appl. Phys. **112,** 013536 (2012).

[61] P. Lecoq, Pushing the limits in time-of-flight PET imaging, IEEE Trans. Radiat. Plasma Med. Sci. **1,** 473 (2017).

[62] W. Chewpraditkul, L. Swiderski, M. Moszynski, T. Szczesniak, A. Syntfeld-Kazuch, C. Wanarak, and P. Limsuwan, Scintillation properties of LuAG:Ce, YAG:Ce and LYSO:Ce crystals for gamma-ray detection, IEEE Trans. Nucl. Sci. **56,** 3800 (2009).

[63] T. Yanagida, Y. Fujimoto, T. Ito, K. Uchiyama, and K. Mori, Development of x-ray-induced afterglow characterization system, Appl. Phys. Express **7,** 0624101 (2014).

[64] S. Y. F. Chu, L. P. Ekström, R. B. Firestone, The Lund/LBNL Nuclear Data Search - Version 2.0 (1999). http://nucleardata.nuclear.lu.se/toi/index.asp

[65] J. Páterek, R. Král, J. Pejchal, R. Prokeš, and M. Nikl, LuAG:Pr codoped with Ho^{3+}: Acceleration of Pr^{3+} decay by energy transfer, Radiat. Meas. **124,** 122 (2019).

[66] P. Kantuptim, T. Kato, D. Nakauchi, N. Kawaguchi, and Y. Yanagida, Scintillation properties of Pr-doped lanthanum pyrosilicate single crystals, Crystals **12,** 459 (2022).

[67] J. Becker, J. Y. Gesland, N. Yu Kirikova, J. C. Krupa, V. N. Makhov, M. Runnea, M. Queffelec, T. V. Uvarova, and G. Zimmera, Fast VUV emission of rare earth ions (Nd^{3+}, Er^{3+}, Tm^{3+}) in wide bandgap crystals, J. Alloys Compd. **275–277,** 205 (1998).

[68] V. Jarý, L. Havlák, M. Buryi, E. Mihóková, V. Babin, J. Bárta, V. Vaněček, Z. Remeš, and M. Nikl, Peculiarities and the red shift of Eu^{2+} luminescence in Gd^{3+}-admixed YAG phosphors, Opt. Mater. **120,** 111464 (2021).

[69] S. Stoll and A. Schweiger, EasySpin, a comprehensive software package for spectral simulation and analysis in EPR, J. Magn. Reson. **178,** 42 (2006).

[70] M. Buryi, V. Babin, V. Laguta, D. A. Spassky, V. Nagirnyi, and V. N. Shlegel, Electron and hole trapping in Li_2MoO_4 cryogenic scintillator, Opt. Mater. **114,** 110971(1–10) (2021).

[71] A. M. Monti, M. Buryi, M. Fasoli, and M. Martini, Anomalous thermal stability of the $[GeO_4]^-$ electron paramagnetic resonance signal and the 110 °C thermally stimulated luminescence peak in natural and synthetic quartz, J. Lumin. **238,** 118263 (2021).

[72] A. M. Monti, M. Buryi, M. Fasoli, and M. Martini, EPR characterization in natural quartz samples of a newly discovered hydrogen related defect and already known germanium related defects, Radiat. Meas. **145,** 106604 (2021).

[73] A. Abragam and B. Bleaney, *Electron Paramagnetic Resonance of Transition Ions* (Clarendon Press, Oxford, 1970), Vol. 1, pp. 560–568.

[74] D. A. Spassky, V. Nagirnyi, V. V. Mikhailin, A. E. Savon, A. N. Belsky, V. V. Laguta, M. Buryi, E. N. Galashov, V. N. Shlegel, I. S. Voronina, and B. I. Zadneprovski, Trap centers in molybdates, Opt. Mater. **35,** 2465 (2013).

[75] M. Buryi, D. A. Spassky, J. Hybler, V. V. Laguta, and M. Nikl, Electron spin resonance study of charge trapping in α-$ZnMoO_4$ single crystal scintillator, Opt. Mater. **47,** 244 (2015).

[76] V. Laguta, M. Buryi, J. Pejchal, V. Babin, and M. Nikl, Hole Self-Trapping in $Y_3Al_5O_{12}$ and $Lu_3Al_5O_{12}$ Garnet Crystals, Phys. Rev. Appl. **10,** 034058 (2018).

[77] M. Buryi, L. Havlák, V. Jarý, J. Bárta, V. Laguta, A. Beitlerová, J. Li, X. Chen, Y. Yuan, Q. Liu, Y. Pan, and M. Nikl, Specific absorption in $Y_3Al_5O_{12}$:Eu ceramics and the role of stable Eu^{2+} in energy transfer processes, J. Mater. Chem. C **8,** 8823 (2020).

[78] D. J. Robbins, The effects of crystal field and temperature on the photoluminescence excitation efficiency of Ce^{3+} in YAG, J. Electrochem. Soc. **126,** 1550 (1979).

[79] See the Supplemental Material at http://link.aps.org/supplemental/10.1103/PhysRevApplied.19.034092 for experimental details and additional data and discussion, including Figs. S1–S11.